Volume 11
Number 28
28 July 2023
Pages 15057–15562

Journal of Materials Chemistry A

Materials for energy and sustainability

rsc.li/materials-a

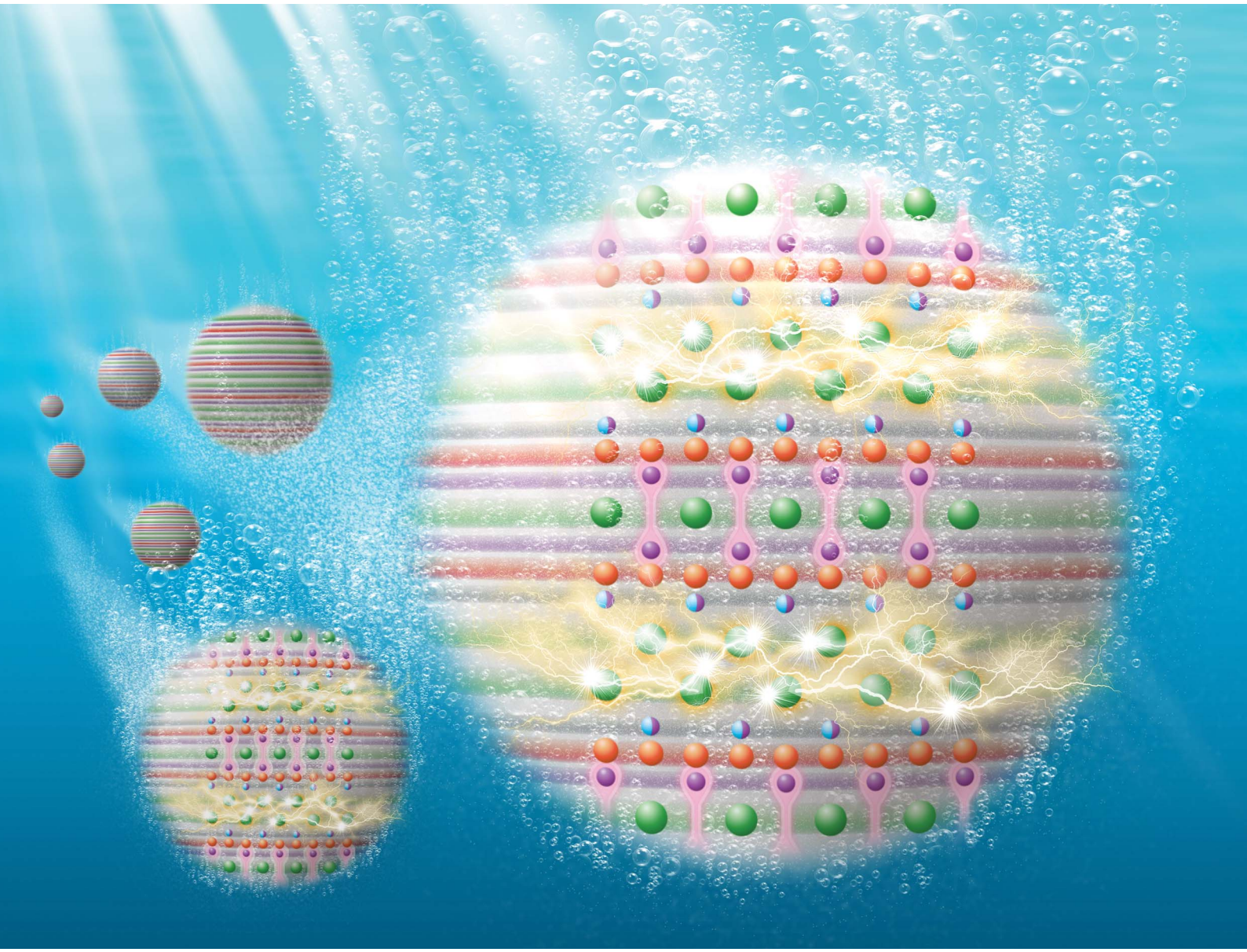

ISSN 2050-7488

ROYAL SOCIETY OF CHEMISTRY

PAPER

Ryu Abe *et al.*

A Sillén oxyhalide $SrBi_3O_4Cl_3$ as a promising photocatalyst for water splitting: impact of the asymmetric structure on light absorption and charge carrier dynamics

10 YEARS ANNIVERSARY

Journal of Materials Chemistry A

ROYAL SOCIETY OF CHEMISTRY

PAPER

View Article Online
View Journal | View Issue

Check for updates

Cite this: J. Mater. Chem. A, 2023, 11, 15159

A Sillén oxyhalide $SrBi_3O_4Cl_3$ as a promising photocatalyst for water splitting: impact of the asymmetric structure on light absorption and charge carrier dynamics†

Hajime Suzuki, ‡[a] Daichi Ozaki,‡[a] Yusuke Ishii, [a] Osamu Tomita, [a] Daichi Kato, [a] Shunsuke Nozawa,[b] Kouichi Nakashima, [c] Akinori Saeki, [d] Hiroshi Kageyama [a] and Ryu Abe *[a]

Bismuth-based oxyhalides with layered Sillén(–Aurivillius) structures have attracted significant attention as photocatalysts. Recent studies have unveiled a part of the structure–property relationship of the materials; however, it has not been fully understood. In the present study, we investigated a Sillén-type oxyhalide $SrBi_3O_4Cl_3$ with single and double halogen layers. Interestingly, $SrBi_3O_4Cl_3$ showed a visible light response up to ~460 nm, whereas $SrBiO_2Cl$ and BiOCl with single and double halogen layers, respectively, did not. Rietveld refinement and STEM-EDX mapping determined the asymmetric Bi occupation in the fluorite $[Sr_{0.5}Bi_{1.5}O_2]$ layer of $SrBi_3O_4Cl_3$, which was derived from the coexistence of the halogen layers. DFT calculations and Madelung potential calculations showed that the asymmetric Bi occupation affords both the Bi–Bi interaction across the single halogen layer and the electrostatic destabilization of Cl in the double halogen layer, probably leading to the narrow bandgap of $SrBi_3O_4Cl_3$. Another merit of possessing the two different halogen layers was revealed by time-resolved microwave conductivity measurements as well as DFT calculations; the spatial separation of the conduction band minimum and valence band maximum based on the coexistence of the halogen layers would promote charge carrier separation. Visible-light-driven Z-scheme water splitting was accomplished using a RuO_2-loaded $SrBi_3O_4Cl_3$ sample as an O_2-evolving photocatalyst. This study provides another option for engineering band structures and promoting the charge carrier separation of layered oxyhalides for efficient water splitting under visible light.

Received 15th February 2023
Accepted 24th May 2023

DOI: 10.1039/d3ta00906h

rsc.li/materials-a

Introduction

Sillén-type oxyhalides possess a layered structure consisting of intergrowth of alternating fluorite $[M_2O_2]$ and halogen [X] layers. Since the first report by Sillén,[1] various compounds that belong to Sillén phases have been reported[2–7] and studied in terms of battery,[8–13] catalysis,[14–18] optical properties,[19–22] photovoltaics,[23–25] photocatalysis,[13–17] *etc.*[18,19] Among them, oxychloride BiOCl with fluorite $[Bi_2O_2]$ and double halogen [Cl] layers is one of the most actively researched materials, along with other analogous BiOBr and BiOI, particularly as a promising photocatalyst for dye degradation,[26–28] selective oxidation reactions,[29–32] and solar energy conversions.[33–36] Although the activity of the BiOCl photocatalyst has been improved *via* various strategies, such as forming heterojunctions[37–39] and engineering defects and facets,[26,27,33] the wide bandgap (~3.5 eV) has restricted its applications under natural sunlight. In addition, it has intrinsic stability problems when employed in harsh reactions, such as water splitting (*i.e.*, water oxidation). Because its valence band maximum (VBM) predominantly consists of Cl-3p orbitals rather than O-2p orbitals, photogenerated holes tend to accumulate and oxidize Cl anions, resulting in irreversible and oxidative deactivation.[40]

In contrast, we have demonstrated that some Sillén oxychlorides, including Pb cations, such as $PbBiO_2Cl$ and $PbBi_3O_4Cl_3$, not only possess narrow bandgaps for visible-light-absorption but also function as stable photocatalysts for water splitting.[41–43] For example, $PbBiO_2Cl$ with fluorite $[PbBiO_2]$ and

[a]Department of Energy and Hydrocarbon Chemistry, Graduate School of Engineering, Kyoto University, Nishikyo-ku, Kyoto 615-8510, Japan. E-mail: ryu-abe@scl.kyoto-u.ac.jp
[b]Photon Factory (PF), Institute of Materials Structure Science (IMSS), High Energy Accelerator Research Organization (KEK), Tsukuba, Ibaraki 305-0801, Japan
[c]Department of Materials Science and Engineering, Graduate School of Science and Engineering, Ibaraki University, 4-12-1, Nakanarusawa, Hitachi, Ibaraki 316-8511, Japan
[d]Department of Applied Chemistry, Graduate School of Engineering, Osaka University, 2-1 Yamadaoka, Suita, Osaka 565-0871, Japan

† Electronic supplementary information (ESI) available. See DOI: https://doi.org/10.1039/d3ta00906h

‡ H. S. and D. O. contributed equally to this work.

single halogen [Cl] layers absorbs visible light up to 500 nm, and can oxidize water to O_2 under visible light without experiencing oxidative deactivation.[41,44,45] Density functional theory (DFT) calculations confirmed that the strong interaction between O-2p and Pb-6s orbitals, with the help of empty Pb-6p, provides an up-shifted VBM consisting of O-2p orbitals dominantly, instead of Cl-3p orbitals, thus endowing $PbBiO_2Cl$ with both a narrow bandgap (~2.5 eV) and high durability against self-oxidative deactivation. In stark contrast, the analogous Sr-counterpart $SrBiO_2Cl$ possesses a much larger bandgap (~3.5 eV). This implies that the presence of Pb cations is vital for the visible-light absorption of such Sillén-type oxychlorides.

Contrary to this expectation, we herein show that Pb-free Sillén oxychloride $SrBi_3O_4Cl_3$ possesses a narrow bandgap (~2.7 eV) and functions as a stable and efficient photocatalyst for water oxidation under visible light. Although this material was first reported by Sillén in 1940,[46] where it has been studied in terms of crystal structure and catalysis,[16,17] there has been no study focusing on photofunctionality, including photocatalysis. The combination of various characterization studies and theoretical approaches in the present study revealed that both the Bi–Bi interactions across the single halogen layer and the electrostatic destabilization of Cl in the double halogen layer arise from the asymmetric Bi occupation in the fluorite $[Sr_{0.5}Bi_{1.5}O_2]$ layer, as well as the coexistence of the halogen layers. These two factors most probably afford a much narrower bandgap than analogous oxychlorides, such as BiOCl and $SrBiO_2Cl$. Furthermore, it was also suggested that the coexistence of the halogen layers in $SrBi_3O_4Cl_3$ promoted spatial charge carrier separation.

Experimental

Materials

Bismuth oxychloride (BiOCl, 95.0%), hydrochloric acid (HCl, 1.0 M), hydrogen hexachloroplatinate hexahydrate ($H_2PtCl_6 \cdot 6H_2O$, 99.9%), iron(III) chloride hexahydrate ($FeCl_3 \cdot 6H_2O$, 99%), iron(III) nitrate enneahydrate ($Fe(NO_3)_3 \cdot 9H_2O$, 99%), iron(III) perchlorate *n*-hydrate ($Fe(ClO_4)_3$, 70% as anhydrous), iron(III) sulfate *n*-hydrate ($Fe_2(SO_4)_3$, 60–80% as anhydrous), methanol (CH_3OH, 99.8%), nitric acid (HNO_3, 1 M), perchloric acid ($HClO_4$, 70% as assay), rhodium oxide (Rh_2O_3, 98.0%), ruthenium chloride *n*-hydrate ($RuCl_3 \cdot nH_2O$, 99.9%), silver nitrate ($AgNO_3$, 99.8%), sodium sulfate (Na_2SO_4, 99.0%), strontium carbonate ($SrCO_3$, 99.99%), sulfuric acid (H_2SO_4, 0.5 M), and titanium oxide (TiO_2, 99.0%) were purchased from FUJIFILM Wako Chemicals. All chemicals were used as received, except for $SrCO_3$ and TiO_2 which were dried at 300 °C for 2 h before use.

Sample synthesis

All samples were synthesized by solid-state reactions. $SrBi_3O_4Cl_3$ was synthesized from a stoichiometric mixture of BiOCl and $SrBiO_2Cl$. First, $SrBiO_2Cl$ was synthesized from a stoichiometric mixture of $SrCO_3$ and BiOCl. The mixture was loaded into an alumina crucible and calcined at 700 °C for 12 h in air. $SrBi_3O_4Cl_3$ can be prepared by heating a stoichiometric mixture of $SrBiO_2Cl$ and BiOCl in an alumina crucible at 600–800 °C for 12 h in air (Fig. S1†). In this study, the $SrBi_3O_4Cl_3$ sample prepared at 700 °C was used. As seen from scanning electron microscopy (SEM) images, the sample has aggregated particles with a plate-like shape with a few hundred nanometers in size (Fig. S2†). The RuO_2 cocatalyst was deposited on $SrBi_3O_4Cl_3$ by an impregnation method. $SrBi_3O_4Cl_3$ was dispersed in a small amount of $RuCl_3$ aqueous solution (0.7 wt% Ru metal) and calcined at 500 °C for 1 h in air.

As an H_2-evolving photocatalyst in Z-scheme water splitting, rhodium-doped strontium titanate ($SrTiO_3:Rh$) was synthesized by a solid-state reaction.[47] A mixture of TiO_2, $SrCO_3$, and Rh_2O_3, with a molar ratio of $Ti:Sr:Rh = 1:1.07$ of 0.01, was calcined in an alumina crucible at 600 °C for 2 h and subsequently at 1000 °C for 10 h with an intermediate ground. A Ru-based cocatalyst was deposited on $SrTiO_3:Rh$ by a photodeposition method.[48] $SrTiO_3:Rh$ was suspended in a methanol aqueous solution (10 vol%, 120 mL) containing $RuCl_3$ (0.7 wt% Ru metal) and irradiated by visible light ($400 < \lambda < 800$ nm) for 2 h.

Characterization

Powder X-ray diffraction (XRD; MiniFlex II, Rigaku, Cu Kα), SEM (NVision 40, Carl Zeiss-SIINT), scanning transmission electron microscopy (STEM; JEOL) with energy-dispersive X-ray spectroscopy (EDX), UV-vis diffuse reflectance spectroscopy (V-650, Jasco), and X-ray photoelectron spectroscopy (XPS; ESCA 5500MT, ULVAC-PHI, Mg Kα) were used to characterize the samples. The XPS binding energies were corrected with respect to the Au 4f peak (84.0 eV). Synchrotron X-ray diffraction (SXRD; BL02B2, SPring-8, Japan, $\lambda = 0.419432$ Å) patterns were collected at room temperature. Indexing of the SXRD patterns and Rietveld refinement were conducted using EXPO2014 and RIETAN-FP programs.[49,50] The VESTA program was used for drawing crystal structures.[51] The maximum entropy method (MEM) analysis was conducted using the Dysnomia program.[52] Time-resolved microwave conductivity (TRMC) measurements were performed using the fourth harmonic generation (FHG at 266 nm, $I_0 = 1.4 \times 10^{15}$ photons per cm^2 per pulse) from an Nd:YAG laser (Spectra Physics, GCR-200, 5–8 ns pulse duration, 10 Hz) as the excitation source. The resonant frequency and microwave power were set to ~9.1 GHz (X-band) and 3 mW.

Electrochemical measurement

Mott–Schottky plots were recorded in a three-electrode cell equipped with a Pt wire counter-electrode and Ag/AgCl reference electrode in a phosphate-buffered solution (0.1 M, pH 6.0) using an electrochemical analyzer (VersaSTAT 4, Princeton Applied Research), with an amplitude of 10 mV and a frequency of 1000 Hz. The electrode was prepared using the squeegee method. A particulate sample with a small amount of water was coated on a fluorine-doped tin oxide (FTO) conductive substrate and dried overnight at room temperature.

Calculation

The partial density of states (PDOS) of $SrBi_3O_4Cl_3$ was calculated using the Cambridge Serial Total Energy Package (CASTEP).[53]

The energy was calculated using the generalized gradient approximation (GGA) of DFT proposed by Perdew, Brurke, and Ernzerhof (PBE). The electronic states were expanded using a plane-wave basis set with a cut-off of 700 eV. The *k*-point meshes were set as 3 × 3 × 1. Before the PDOS calculations, geometry optimization was performed using the Broyden–Fletcher–Goldfarb–Shanno (BFGS) algorithm. The crystal orbital Hamilton populations (COHP) were calculated using the Quantum Espresso package[54] and the Local-Orbital Basis Suite Toward Electronic-Structure Reconstruction (LOBSTER) package.[55] The Perdew–Burke–Ernzerhof functional for solids (PBEsol) generalized gradient approximation (GGA) was used as the exchange-correlation functional. A cutoff energy of 100 Ry (~1361 eV) and 6 × 6 × 2 *k*-points were used. We confirmed that the calculated PDOS (Fig. S3†) was similar to that obtained using the calculation described above using the CASTEP (Fig. 5).

Photocatalytic reactions

Photocatalytic reactions were performed in an overhead irradiation-type Pyrex glass vessel connected to a closed gas circulation system. The system was degassed and purged with Ar gas before each photocatalytic reaction. A Xe lamp (LAMP HOUSE R300-3J, Eagle engineering, 300 W) equipped with a cold mirror (CM-1, Kenko) and a cut-off filter (L-42, HOYA) was used as a visible-light ($400 < \lambda < 800$ nm) source. As for UV-vis light ($300 < \lambda < 500$ nm) irradiation, the Xe lamp equipped with only a cold mirror (CM-2, Kenko) was used. The evolved gases were analyzed using online gas chromatography (GC-8A, Shimadzu, thermal conductivity detector, 5 Å molecular sieve column packing) that uses Ar carrier gas. For O_2 evolution reactions, the photocatalyst (100 mg) was suspended in an aqueous solution of $FeCl_3$, $Fe(NO_3)_3$, $Fe_2(SO_4)_3$ or $Fe(ClO_4)_3$ (5 mM Fe^{3+}, 120 mL, pH 2.4, adjusted by using HCl, HNO_3, H_2SO_4 or $HClO_4$) and irradiated with visible light. For the H_2 evolution reactions, the photocatalyst (100 mg) was suspended in an aqueous methanol solution (10 vol%, 120 mL) and irradiated with UV-vis light. A Pt cocatalyst (1 wt%) was loaded onto the photocatalyst by an *in situ* photodeposition method using H_2PtCl_6 as a precursor. Z-scheme overall water splitting, employing $RuO_2/SrBi_3O_4Cl_3$ and $Ru/SrTiO_3:Rh$ as the O_2-evolving and H_2-evolving photocatalysts, respectively, was conducted. The two photocatalysts (50 mg each) were suspended in an aqueous solution of $FeCl_3$ or $Fe_2(SO_4)_3$ (2 mM Fe^{3+}, 120 mL, pH 2.4, adjusted by HCl or H_2SO_4) and irradiated with visible light. The apparent quantum efficiencies (AQE) for Z-scheme water splitting were measured using a similar experimental setting. A Xe lamp equipped with both a CM-1 cold mirror and bandpass filter ($\lambda = 420 \pm 5$ nm, ASAHI) was used as the light source. The AQE was calculated using the following equation:

$$\mathrm{AQE}\ (\%) = 100 \times A \times R/I$$

where A is the number of photons required to generate one molecule of the product (*i.e.*, eight for O_2 and four for H_2 evolution), R is the rate of gas evolution, and I is the number of incident photons (101.6 mW).

Results and discussion

Synthesis and crystal structure analysis

Rietveld refinement of the $SrBi_3O_4Cl_3$ sample synthesized was performed using the SXRD pattern collected at room temperature. All diffraction peaks within $2\theta = 2$–$24°$ were indexed to the tetragonal system. Based on previous reports,[17] space group *I*4/*mmm* (#139) was adopted for Rietveld refinement. Reliability factors converged to $R_p = 0.0795$, $R_{wp} = 0.1301$, $R_B = 0.0337$, $R_F = 0.0251$, and $\chi^2 = 3.240$. The final Rietveld plot and the refined crystal structure are shown in Fig. 1 and S4.† The refined parameters (Table S1†) were similar to those in a previous study,[17] whereas in the present study, the positions of the cations were individually refined for Bi and Sr to obtained a more accurate structure. There are two Bi/Sr sites in the unit cell, derived from the asymmetric layered structure, that is, the fluorite $[Sr_{0.5}Bi_{1.5}O_2]$ layer sandwiched between the single-halogen [Cl] and double-halogen [Cl_2] layers. Rietveld refinement indicated that the Bi/Sr1 site adjacent to the [Cl] layer is almost fully occupied by Bi^{3+}, whereas Bi/Sr2 next to the [Cl_2] layer is shared almost equally by Bi^{3+} and Sr^{2+} (see Table 1). The electron density distribution obtained by MEM analysis (Fig. S5†) shows that the Bi/Sr1–O1 bond has a more covalent bonding character than the Bi/Sr2–O1 bond, which corresponds to the difference in occupations. Although the preferential occupancy of Bi^{3+} in the Bi/Sr1 site is also seen in the previous reports on XRD-based structural analysis,[17] the detailed STEM observation in the present study provides direct evidence. As seen in Fig. 2, a periodic atomic arrangement agreeing with the refined crystal structure was observed in the high-angle annular dark field STEM (HAADF-STEM) and annular bright-field STEM (ABF-STEM) images in the direction of [100]. The elemental mapping (Fig. 2d) further confirmed the validity of the refined crystal structure. Importantly, the occupancies of the Bi/Sr1 and Bi/Sr2 sites are in good agreement with those obtained by Rietveld refinement (Table 1). The preferential occupancy of Bi^{3+} in the Bi/Sr1 site can be explained by Pauling's second rule. The bond valence sum of Bi and Sr cations in the two sites was

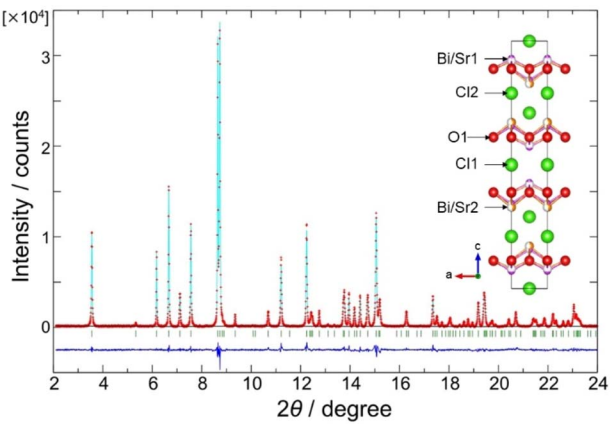

Fig. 1 Final Rietveld plot for $SrBi_3O_4Cl_3$ using the SXRD pattern collected at room temperature; $R_p = 0.0795$, $R_{wp} = 0.1301$ $R_B = 0.0337$, $R_F = 0.0251$, and $\chi^2 = 3.240$.

Table 1 Site occupancies in $SrBi_3O_4Cl_3$ obtained by Rietveld refinement (Fig. 1) and STEM-EDX (Fig. 2)

Atom	Rietveld refinementi	EDX
Bi/Sr1	Bi: 0.972(2)	Bi: 0.96(4)
	Sr: 0.028(2)	Sr: 0.04(2)
Bi/Sr2	Bi: 0.528(2)	Bi: 0.53(3)
	Sr: 0.472(2)	Sr: 0.47(4)

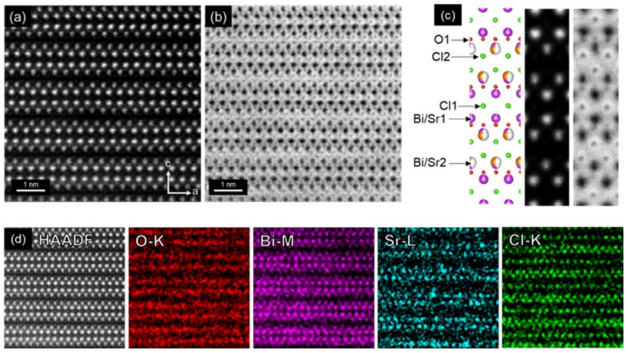

Fig. 2 STEM images of $SrBi_3O_4Cl_3$ in the direction of [100]. (a) HAADF, (b) ABF, (c) their enlarged images with the crystal structure, and (d) EDX elemental maps of $SrBi_3O_4Cl_3$.

calculated (Table S2†), where Sr cations in Bi/Sr1 were significantly overbonded. Such a large overbonding indicates that it is difficult for Sr cations to occupy the Bi/Sr1 site. As will be discussed later, the asymmetric distribution of Bi^{3+} cations in the fluorite layer of $SrBi_3O_4Cl_3$ is most likely the key to its narrower bandgap than that of analogous materials, such as $SrBiO_2Cl$.

Band structure of $SrBi_3O_4Cl_3$ and other analogues

Fig. 3a and b show the diffused reflectance spectra and the estimated band levels, respectively, of $SrBi_3O_4Cl_3$, $SrBiO_2Cl$, and BiOCl, whose refined crystal structures are shown in Fig. 4. The band levels were estimated based on a combination of bandgaps and flat-band potentials determined from the reflectance

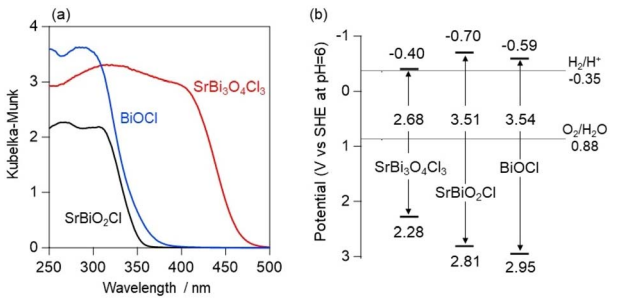

Fig. 3 (a) Diffuse reflectance spectra of $SrBi_3O_4Cl_3$, $SrBiO_2Cl$, and BiOCl. (b) The band levels estimated from the diffuse reflectance spectra and MS plots (Fig. S7†). The band levels of BiOCl were estimated from the reported MS plot.[56] Flat-band potentials are assumed to be located just below the CBMs due to the n-type nature of these materials.

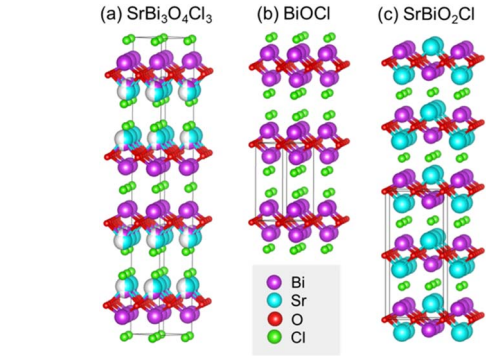

Fig. 4 Refined crystal structure of $SrBi_3O_4Cl_3$, along with BiOCl[57] and $SrBiO_2Cl$.[58] For clarity, the Bi/Sr1 site being next to the single [Cl] layer is fully occupied by Bi^{3+}, whereas the Bi/Sr2 next to the double [Cl] layer is shared equally by Bi^{3+} and Sr^{2+}.

spectra (Fig. S6†) and Mott–Schottky (MS) plots (Fig. S7†), respectively. Despite their similar compositions and structures, only $SrBi_3O_4Cl_3$ possesses a narrow bandgap (2.68 eV), enabling visible absorption, which is derived from both the positively shifted CBM and the negatively shifted VBM compared to others.

Fig. 5 shows the density of states (DOS) and partial DOS (PDOS) of $SrBi_3O_4Cl_3$, calculated based on the assumption that Bi^{3+} and Sr^{2+} are ordered in the Bi/Sr2 site, whereas the Bi/Sr1 site is fully occupied by Bi^{3+} in a $\sqrt{2} \times \sqrt{2} \times 1$ supercell (Fig. S8†). The orbital distributions of the CBM and VBM of $SrBi_3O_4Cl_3$ are shown in Fig. 6. Given the refined crystal structures (Fig. 4), the significantly lowered CBM of $SrBi_3O_4Cl_3$ can probably be explained by Bi–Bi interactions across the single halogen layer. As shown in Fig. 5 and S9,† the DOS around the CBM is formed exclusively by Bi 6p orbitals at the Bi/Sr1 site, which Bi^{3+} almost fully occupies. In addition, an obvious interaction between the

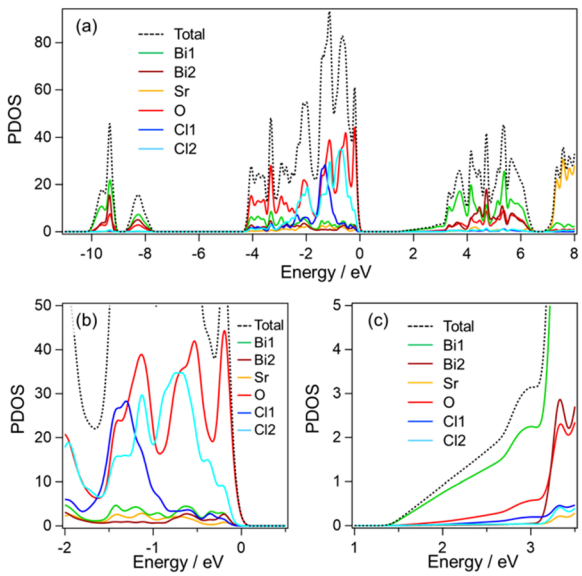

Fig. 5 (a) DOS and PDOS of $SrBi_3O_4Cl_3$. (b) and (c) their close-ups at around the VBM and CBM, respectively.

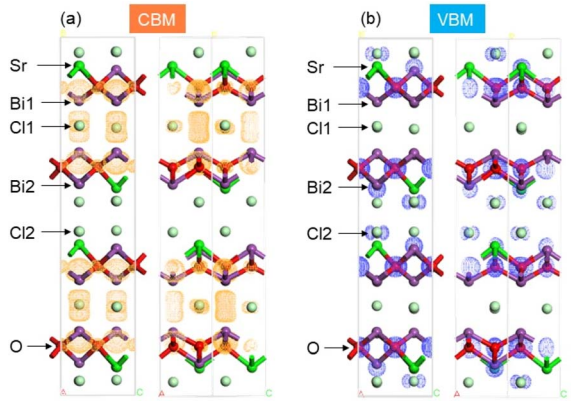

Fig. 6 Orbital distributions of the CBM ((a) orange) and VBM ((b) blue) of $SrBi_3O_4Cl_3$ estimated by DFT calculations (isosurface value: 0.01 e $Å^{-3}$), which are viewed from two different directions corresponding to the (110) (left) and (100) (right) directions for the refined structure (Fig. 1).

two Bi^{3+} ions across the single Cl anion layer can be observed in the visualized CBM (Fig. 6). The interaction was evaluated using the crystal orbital Hamilton population (COHP), in which positive and negative values indicate the bonding and antibonding nature, respectively (Fig. S10†). The COHP for the interaction of Bi 6pz–Bi 6pz reveals the bonding nature at the CBM; the Bi-6pz orbitals interact with each other across the single halogen layer, forming bonding and antibonding states. The bonding states, which are more positive than the nonbonding states of the Bi-6pz orbitals, significantly lowered the CBM of $SrBi_3O_4Cl_3$. Such Bi–Bi interactions can be rationalized by the coordination environment of the Bi/Sr1 site in $SrBi_3O_4Cl_3$, as previously discussed. In the fluorite $[Sr_{0.5}Bi_{1.5}O_2]$ layer, the Bi/Sr1 site adjacent to the [Cl] layer is almost fully occupied by Bi^{3+}, whereas Bi/Sr2 next to the $[Cl_2]$ layer is shared almost equally by Bi^{3+} and Sr^{2+}. No Cl anion is coaxially arranged with Bi^{3+} in Bi/Sr1, whereas coaxially arranged Bi^{3+} exists across the [Cl] layer. Although the coordination environment of Bi/Sr in $SrBiO_2Cl$ (having single Cl layers only) is similar to that in Bi/Sr1 of $SrBi_3O_4Cl_3$, the occupancies of the cations are different from each other. Rietveld refinement of $SrBiO_2Cl$ in a previous report[58] indicated that Bi^{3+} and Sr^{2+} in the Bi/Sr site are ordered, as shown in Fig. 4. In the fluorite $[SrBiO_2]$ layer, Bi^{3+} and Sr^{2+} are distributed in a balanced manner toward the halogen layer. This cation distribution causes the Bi^{3+} cation to face the coaxially arranged Sr^{2+} cation across the [Cl] layer, preventing Bi–Bi interaction across the Cl layer (Fig. S11†). To evaluate the impact of Bi–Bi interactions on the band structure, additional DFT calculations were conducted using a hypothetical model of $SrBi_3O_4Cl_3$ where the Bi/Sr1 site is orderly and equally shared by Bi^{3+} and Sr^{2+} whereas the Bi/Sr2 site is solely occupied by Bi^{3+} (Fig. S12†), where the presence of Sr^{2+} in the Bi/Sr1 site drastically increases the bandgap from 1.4 to 2.6 eV. As for BiOCl, the double [Cl] layers increased the distance between the vertically arranged Bi^{3+}, weakening their interaction (Fig. S13†).

As shown in Fig. 5, the VBM of $SrBi_3O_4Cl_3$ is mainly composed of O-2p orbitals along with a contribution of the Cl-3p orbitals of Cl2 in the double layer. This sizable contribution of Cl-3p in $SrBi_3O_4Cl_3$ is in stark contrast to $SrBiO_2Cl$ having single halogen layers only, where the contribution of Cl-3p to the VBM is negligible (Fig. S14†). In previous studies, we have revealed that the ionic orbital energy levels of each anion, which can be calculated from the sum of the electron affinity and the Madelung potential at each crystallographic site, can appropriately reproduce the features of the valence band PDOS obtained from DFT calculations.[59] Fig. 7 shows the ionic energy levels of each Cl anion in these compounds, where the ionic energy level of Cl2 in the double layer of $SrBi_3O_4Cl_3$ exhibits the highest value, while those of Cl anions in $SrBiO_2Cl$ and BiOCl exhibit approximately the same and low values. The highest value indicates that the Cl2 anion in $SrBi_3O_4Cl_3$ was electrostatically destabilized. Cl anions are more destabilized in $SrBi_3O_4Cl_3$ than in $SrBiO_2Cl$ due to the strong repulsion between Cl anions in the double layer. Although such destabilization is also expected for Cl anions in the Cl double layer of BiOCl, their ionic energy level is significantly lower than that of $SrBi_3O_4Cl_3$. This difference in the ionic energies of Cl anions in Cl double layers can be understood by considering the valence state of the surrounding cations. While the Cl anions in the double layer of $SrBi_3O_4Cl_3$ are surrounded by four Sr^{2+}/Bi^{3+} cations (*i.e.*, a positive charge of 2.5) owing to the asymmetric Bi occupation in the fluorite $[Sr_{0.5}Bi_{1.5}O_2]$ layer, those in BiOCl are surrounded by four Bi^{3+} cations, resulting in a higher positive charge to stabilize Cl anions. The COHP for the Bi2–O and Bi2–Cl2 interactions (Fig. S15†) shows an antibonding nature at the VBM; the Cl and O orbitals probably interact with each other through the interaction with Bi orbitals, forming the elevated VBM of $SrBi_3O_4Cl_3$. In conclusion, the most negative VBM level of $SrBi_3O_4Cl_3$ can probably be rationalized by the destabilization of Cl2 anions in $SrBi_3O_4Cl_3$ and the accompanying sizable contribution of the Cl-3p of Cl2 to the VBM rather than that of Cl1. In future studies, a more systematic investigation of a series of related layered oxyhalides needs to be conducted to confirm the origin of the elevated VBM of $SrBi_3O_4Cl_3$ and, thereby, provide a guiding principle for controlling band levels by designing halogen layers (*e.g.*, change in the proportion of single and double halogen layers).

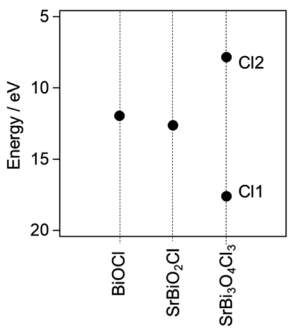

Fig. 7 Ionic energy levels of each halogen site in $SrBi_3O_4Cl_3$, calculated from the sum of the Madelung potentials at the Cl site and electron affinity, along with those of BiOCl and $SrBiO_2Cl$. The Madelung potentials for $SrBi_3O_4Cl_3$ were calculated from the refined structure (Fig. 1 and Table S1†).

Carrier dynamics and photocatalytic reactions

Before discussing the photocatalytic reactions, we evaluated the carrier dynamics of $SrBi_3O_4Cl_3$ by TRMC, which gives the signal of the product of the charge carrier generation efficiency φ and the sum of the charge carrier mobilities $\Sigma\mu$. As shown in Fig. 8, $SrBi_3O_4Cl_3$ shows a significantly higher TRMC signal than the others after excitation at 266 nm, despite a similar, high photoabsorption at this wavelength among all the samples. The product of the maximum signal intensity and lifetime, which has been previously reported to well correlate with the photocatalytic activities of some oxyhalide photocatalysts,[44,45] is more than an order of magnitude larger than that of BiOCl and $SrBiO_2Cl$ (Fig. S16 and Table S3†). This superior carrier dynamics of $SrBi_3O_4Cl_3$ is probably derived from the spatial separation of the CBM and VBM (Fig. 6), which is regarded as an effective strategy to promote charge separation,[60–62] as also suggested in analogous $PbBi_3O_4Cl_3$.[56] The present result shows that the coexistence of single and double halogen layers in $SrBi_3O_4Cl_3$ not only provides visible light response but also improved carrier separation and suppression of charge recombination.

$SrBi_3O_4Cl_3$ showed a negligibly low H_2 evolution activity (Fig. S17†), as expected from the slightly more negative CBM compared to the water reduction potential (Fig. 3b). In contrast, it exhibited a reasonable activity for O_2 evolution from water in the presence of an appropriate electron acceptor, such as Fe^{3+}. Fig. 9a shows the time course of photocatalytic O_2 evolution in the presence of an Fe^{3+} electron acceptor with various counter anions; the O_2 evolution rates strongly depend on the type of counter anions. This influence of anions has also been reported for other photocatalysts.[41,63,64] Although $FeCl_3$ provided the highest rate, we noticed slight but obvious impurity peaks derived from BiOCl after the reaction, except for $Fe_2(SO_4)_3$ (Fig. 9b). The emergence of such a small amount of BiOCl was also observed under dark conditions, suggesting that the change mainly occurred chemically and not photochemically. The following evaluations were conducted using mainly $Fe_2(SO_4)_3$, which does not provide a BiOCl phase at all, to avoid the possible influence of the BiOCl phase.

The loading of RuO_x cocatalysts on $SrBi_3O_4Cl_3$ increased the O_2 evolution rate from aqueous Fe^{3+} solution in a similar fashion to other oxyhalides.[41,56,65] The formation of RuO_2 was confirmed by XAFS and XPS measurements (Fig. 10a and S18†). RuO_2-loaded $SrBi_3O_4Cl_3$ ($RuO_2/SrBi_3O_4Cl_3$) exhibited steady O_2 evolution repeatedly at least three times from aqueous solutions of $Fe_2(SO_4)_3$ (Fig. 10b). Importantly, an almost stoichiometric amount of O_2 (150 μmol) estimated from the amount of introduced Fe^{3+} was evolved, strongly suggesting that O_2 evolution in this system was not significantly suppressed by the backward oxidation of Fe^{2+} to Fe^{3+} by holes.[66] A Z-scheme overall water splitting system was constructed using a combination of $RuO_2/SrBi_3O_4Cl_3$ and $Ru/SrTiO_3:Rh$,[47,48] respectively, as O_2- and H_2-

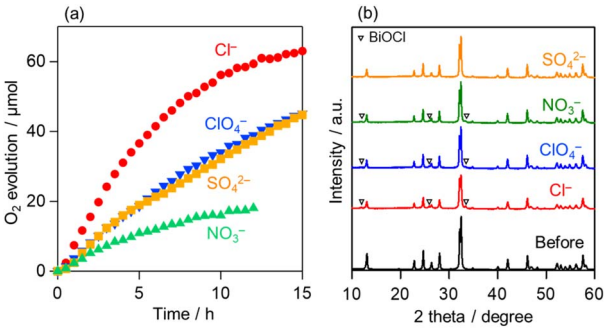

Fig. 9 (a) Time courses of photocatalytic O_2 evolution on $SrBi_3O_4Cl_3$ under visible light ($400 < \lambda < 800$ nm) from an aqueous solution of $FeCl_3$, $Fe(NO_3)_3$, $Fe_2(SO_4)_3$ or $Fe(ClO_4)_3$ (5 mM as Fe^{3+}, 120 mL, pH 2.4). (b) XRD patterns of $SrBi_3O_4Cl_3$ after the reactions.

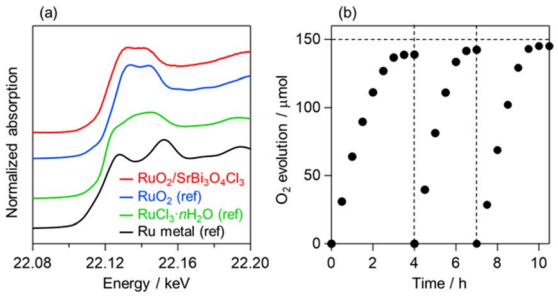

Fig. 10 (a) Ru K-edge XANES spectra for the $SrBi_3O_4Cl_3$ sample loaded with Ru species. (b) Third-cycle test of photocatalytic O_2 evolution on $RuO_2/SrBi_3O_4Cl_3$ under visible light ($400 < \lambda < 800$ nm) from an aqueous solution of $Fe_2(SO_4)_3$ (5 mM as Fe^{3+}, 120 mL, pH 2.4).

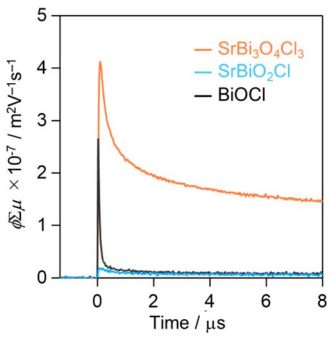

Fig. 8 TRMC transients ($\varphi\Sigma\mu$) of $SrBi_3O_4Cl_3$, $SrBiO_2Cl$, and BiOCl after excitation at 266 nm.

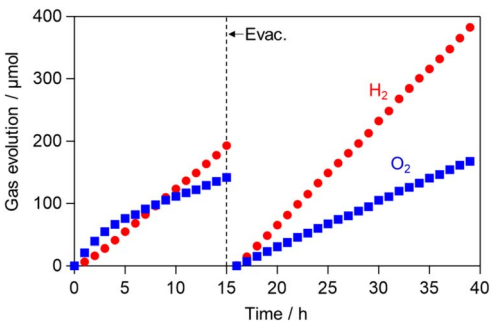

Fig. 11 Z-scheme overall water splitting using $RuO_2/SrBi_3O_4Cl_3$ as an O_2-evolving photocatalyst and $Ru/SrTiO_3:Rh$ as a H_2-evolving photocatalyst under visible light ($400 < \lambda < 800$ nm) in an aqueous $Fe_2(SO_4)_3$ solution (2 mM as Fe^{3+}, 120 mL, pH 2.4).

evolving photocatalysts. As shown in Fig. 11, an excess amount of O_2 was generated at the initial stage because of the higher concentration of Fe^{3+} (*vs.* Fe^{2+}), which functioned as the electron acceptor for $RuO_2/SrBi_3O_4Cl_3$. With increasing time, the rate of H_2 evolution gradually increased as a result of the increased concentration of Fe^{2+} and finally approached an almost stoichiometric value (*i.e.*, $H_2 : O_2 = 2 : 1$). At 420 nm, the AQE was 0.3% and 0.9% with $Fe_2(SO_4)_3$ and $FeCl_3$ (see Fig. S19†), respectively. Although the value is not so high compared with the reported ones,[67] we expect that further optimizations will improve the performance of photocatalytic water splitting.

Conclusions

In the present work, we studied a Sillén phase $SrBi_3O_4Cl_3$ with single/double halogen layers to investigate the structure–property relationship of layered bismuth oxyhalides. Rietveld refinement and STEM-EDX mapping of $SrBi_3O_4Cl_3$ confirmed the asymmetric occupation of Bi in the fluorite $[Sr_{0.5}Bi_{1.5}O_2]$ layer, which was caused by the coexistence of two different halogen layers. Interestingly, only $SrBi_3O_4Cl_3$ showed a visible light response (bandgap: 2.68 eV), whereas $SrBiO_2Cl$ and BiOCl did not. Theoretical investigations suggest that both the Bi–Bi interaction across the single halogen layer and the electrostatic destabilization of Cl in the double halogen layer lead to the narrow bandgap of $SrBi_3O_4Cl_3$. TRMC measurements and DFT calculations suggested another advantage of possessing two different halogen layers in $SrBi_3O_4Cl_3$: the spatial separation of the CBM and VBM based on the coexistence of halogen layers probably promotes charge-carrier separation. The loading of RuO_2 cocatalysts significantly improved the O_2 evolution activity of $SrBi_3O_4Cl_3$, and the RuO_2-loaded $SrBi_3O_4Cl_3$ sample functioned as an O_2-evolving photocatalyst for Z-scheme water splitting under visible light. This study provides another option for engineering the band structures and charge-carrier dynamics of layered oxyhalides. In particular, the Bi–Bi interlayer interactions may have already played an important role in previously reported oxyhalide photocatalysts with a single halogen layer.

Conflicts of interest

There are no conflicts to declare.

Acknowledgements

This work was supported by JST CREST (JPMJCR1421), the JSPS Core-to-Core Program (JPJSCCA20200004), JSPS KAKENHI (JP20H00398) in Grant-in-Aid for Scientific Research (A), JSPS KAKENHI (JP16H06438) in Grant-in-Aid for Scientific Research on Innovative Area "Mixed Anion", JSPS KAKENHI (JP17H06439 and JP17H06438) in Scientific Research on Innovative Area "Innovations for Light-Energy Conversion (I4LEC)" and KAKENHI (JP21K14719 and JP21K20556) in Grant-in-Aid for Early-Career Scientists and Research Activity Start-up. This work was also supported by the Tokuyama Science Foundation and Yashima Environment Technology Foundation. A part of this work was supported by the Advanced Characterization Platform and AIST Nanocharacterization Facility (ANCF) Platform as a program of the "Nanotechnology Platform" (JPMXP09A20KU0355). We are also grateful to Takaaki Toriyama of Kyushu University for helpful support in the STEM analysis. Synchrotron experiments were performed at SPring-8 BL02B2 of JASRI (2020A0824 and 2022A1081). The authors are also indebted to the technical division of the Institute for Catalysis, Hokkaido University, for their help in building the experimental equipment.

Notes and references

1 L. G. Sillen, *Naturwissenschaften*, 1938, **26**, 612–613.
2 L. G. Sillen, *Naturwissenschaften*, 1942, **30**, 318–324.
3 D. O. Charkin, O. S. Morozov, E. A. Ul'yanova, P. S. Berdonosov, V. A. Dolgikh, C. Dickinson, W. Zhou and P. Lightfoot, *Solid State Sci.*, 2006, **8**, 1029–1034.
4 A. Pfitzner and P. Pohla, *Z. Anorg. Allg. Chem.*, 2009, **635**, 1157–1159.
5 J. F. Vigier, C. Renard, N. Henry, A. Laplace and F. Abraham, *Inorg. Chem.*, 2012, **51**, 4352–4358.
6 D. O. Charkin, P. S. Berdonosov, V. A. Dolgikh and P. Lightfoot, *J. Solid State Chem.*, 2003, **175**, 316–321.
7 M. Schmidt, H. Oppermann, C. Hennig, R. W. Henn, E. Gmelin, N. Söger and M. Binnewies, *Z. Anorg. Allg. Chem.*, 2000, **626**, 125–135.
8 D. H. Nam and K. S. Choi, *J. Am. Chem. Soc.*, 2017, **139**, 11055–11063.
9 Y. Myung, J. Choi, F. Wu, S. Banerjee, E. H. Majzoub, J. Jin, S. U. Son, P. V. Braun and P. Banerjee, *ACS Appl. Mater. Interfaces*, 2017, **9**, 14187–14196.
10 D.-H. Nam, M. A. Lumley and K.-S. Choi, *Chem. Mater.*, 2019, **31**, 1460–1468.
11 J. Sun, Q. Sun, A. Plewa, Y. Wang, L. He, F. Zheng, C. Chen, W. Zajac, J. Molenda, K. Zeng and L. Lu, *Angew. Chem., Int. Ed.*, 2020, **59**, 8991–8997.
12 J. Wang, B. Wang and B. Lu, *Adv. Energy Mater.*, 2020, **10**, 2000884.
13 V. Ahuja, S. Singh, R. Vengarathody and P. Senguttuvan, *J. Phys. Chem. C*, 2021, **125**, 17622–17628.
14 H. Li, F. Qin, Z. Yang, X. Cui, J. Wang and L. Zhang, *J. Am. Chem. Soc.*, 2017, **139**, 3513–3521.
15 Q. Yuan, W. Gong, Y. Ye, J. Liu, Y. Lin, C. Chen, H. Zhang, P. Li, W. Cheng, X. Wei and C. Liang, *ChemCatChem*, 2019, **11**, 2676–2682.
16 W. Ueda, S.-W. Lin and I. Tohmoto, *Catal. Lett.*, 1997, **44**, 241–245.
17 L. S. Wen, K. Y. Chul and U. Wataru, *Bull. Chem. Soc. Jpn.*, 1998, **71**, 1089–1094.
18 N. Kijima, K. Matano, M. Saito, T. Oikawa, T. Konishi, H. Yasuda, T. Sato and Y. Yoshimura, *Appl. Catal., A*, 2001, **206**, 237–244.
19 A. Aliev, J. Olchowka, M. Colmont, E. Capoen, C. Wickleder and O. Mentré, *Inorg. Chem.*, 2013, **52**, 8427–8435.
20 J. Olchowka, H. Kabbour, M. Colmont, M. Adlung, C. Wickleder and O. Mentre, *Inorg. Chem.*, 2016, **55**, 7582–7592.

21 Y. Kitagawa, J. Ueda, K. Arai, H. Kageyama and S. Tanabe, *J. Appl. Phys.*, 2021, **129**, 183104.
22 X. Zhang, Y. Zhang, Z. Feng, J. Zhao, Z. Yang, X. Wang and W. Wang, *Chem. Eng. J.*, 2022, **428**, 131235.
23 H. Kunioku, M. Higashi and R. Abe, *Sci. Rep.*, 2016, **6**, 32664.
24 R. L. Z. Hoye, L. C. Lee, R. C. Kurchin, T. N. Huq, K. H. L. Zhang, M. Sponseller, L. Nienhaus, R. E. Brandt, J. Jean, J. A. Polizzotti, A. Kursumovic, M. G. Bawendi, V. Bulovic, V. Stevanovic, T. Buonassisi and J. L. MacManus-Driscoll, *Adv. Mater.*, 2017, **29**, 1702176.
25 T. N. Huq, L. C. Lee, L. Eyre, W. Li, R. A. Jagt, C. Kim, S. Fearn, V. Pecunia, F. Deschler, J. L. MacManus-Driscoll and R. L. Z. Hoye, *Adv. Funct. Mater.*, 2020, **30**, 1909983.
26 J. Jiang, K. Zhao, X. Xiao and L. Zhang, *J. Am. Chem. Soc.*, 2012, **134**, 4473–4476.
27 M. Guan, C. Xiao, J. Zhang, S. Fan, R. An, Q. Cheng, J. Xie, M. Zhou, B. Ye and Y. Xie, *J. Am. Chem. Soc.*, 2013, **135**, 10411–10417.
28 L. Liu, Y. Sun, X. Cui, K. Qi, X. He, Q. Bao, W. Ma, J. Lu, H. Fang, P. Zhang, L. Zheng, L. Yu, D. J. Singh, Q. Xiong, L. Zhang and W. Zheng, *Nat. Commun.*, 2019, **10**, 4472.
29 G. Qiu, T. Wang, X. Li, X. Tao and B. Li, *Ind. Eng. Chem. Res.*, 2020, **59**, 11517–11526.
30 B. Li, L. Shao, R. Wang, X. Dong, F. Zhao, P. Gao and Z. Li, *J. Mater. Chem. A*, 2018, **6**, 6344–6355.
31 F. Xie, Y. Zhang, X. He, H. Li, X. Qiu, W. Zhou, S. Huo and Z. Tang, *J. Mater. Chem. A*, 2018, **6**, 13236–13243.
32 Y. Wu, B. Yuan, M. Li, W. H. Zhang, Y. Liu and C. Li, *Chem. Sci.*, 2015, **6**, 1873–1878.
33 H. Li, J. Shang, H. Zhu, Z. Yang, Z. Ai and L. Zhang, *ACS Catal.*, 2016, **6**, 8276–8285.
34 M. Li, S. Yu, H. Huang, X. Li, Y. Feng, C. Wang, Y. Wang, T. Ma, L. Guo and Y. Zhang, *Angew. Chem., Int. Ed.*, 2019, **58**, 9517–9521.
35 Y. Shiraishi, M. Hashimoto, K. Chishiro, K. Moriyama, S. Tanaka and T. Hirai, *J. Am. Chem. Soc.*, 2020, **142**, 7574–7583.
36 Y. Shi, J. Li, C. Mao, S. Liu, X. Wang, X. Liu, S. Zhao, X. Liu, Y. Huang and L. Zhang, *Nat. Commun.*, 2021, **12**, 5923.
37 Y. Yu, C. Cao, H. Liu, P. Li, F. Wei, Y. Jiang and W. Song, *J. Mater. Chem. A*, 2014, **2**, 1677–1681.
38 T. B. Li, G. Chen, C. Zhou, Z. Y. Shen, R. C. Jin and J. X. Sun, *Dalton Trans.*, 2011, **40**, 6751–6758.
39 L. Sun, L. Xiang, X. Zhao, C.-J. Jia, J. Yang, Z. Jin, X. Cheng and W. Fan, *ACS Catal.*, 2015, **5**, 3540–3551.
40 H. Kunioku, M. Higashi, O. Tomita, M. Yabuuchi, D. Kato, H. Fujito, H. Kageyama and R. Abe, *J. Mater. Chem. A*, 2018, **6**, 3100–3107.
41 H. Suzuki, H. Kunioku, M. Higashi, O. Tomita, D. Kato, H. Kageyama and R. Abe, *Chem. Mater.*, 2018, **30**, 5862–5869.
42 C. Zhong, D. Kato, K. Ogawa, C. Tassel, F. Izumi, H. Suzuki, S. Kawaguchi, T. Saito, A. Saeki, R. Abe and H. Kageyama, *Inorg. Chem.*, 2021, **60**, 15667–15674.
43 A. Nakada, D. Kato, R. Nelson, H. Takahira, M. Yabuuchi, M. Higashi, H. Suzuki, M. Kirsanova, N. Kakudou, C. Tassel, T. Yamamoto, C. M. Brown, R. Dronskowski, A. Saeki, A. Abakumov, H. Kageyama and R. Abe, *J. Am. Chem. Soc.*, 2021, **143**, 2491–2499.
44 H. Suzuki, S. Kanno, M. Hada, R. Abe and A. Saeki, *Chem. Mater.*, 2020, **32**, 4166–4173.
45 H. Suzuki, M. Higashi, H. Kunioku, R. Abe and A. Saeki, *ACS Energy Lett.*, 2019, **4**, 1572–1578.
46 L. G. Sillén, *Naturwissenschaften*, 1940, **28**, 396–397.
47 R. Konta, T. Ishii, H. Kato and A. Kudo, *J. Phys. Chem. B*, 2004, **108**, 8992–8995.
48 Y. Sasaki, A. Iwase, H. Kato and A. Kudo, *J. Catal.*, 2008, **259**, 133–137.
49 A. Altomare, C. Cuocci, C. Giacovazzo, A. Moliterni, R. Rizzi, N. Corriero and A. Falcicchio, *J. Appl. Crystallogr.*, 2013, **46**, 1231–1235.
50 F. Izumi and K. Momma, *Solid State Phenom.*, 2007, **130**, 15–20.
51 K. Momma and F. Izumi, *J. Appl. Crystallogr.*, 2011, **44**, 1272–1276.
52 K. Momma, T. Ikeda, A. A. Belik and F. Izumi, *Powder Diffr.*, 2013, **28**, 184–193.
53 S. J. Clark, M. D. Segall, C. J. Pickard, P. J. Hasnip, M. I. J. Probert, K. Refson and M. C. Payne, *Z. Kristallogr.*, 2005, **220**, 567–570.
54 P. Giannozzi, S. Baroni, N. Bonini, M. Calandra, R. Car, C. Cavazzoni, D. Ceresoli, G. L. Chiarotti, M. Cococcioni, I. Dabo, A. Dal Corso, S. de Gironcoli, S. Fabris, G. Fratesi, R. Gebauer, U. Gerstmann, C. Gougoussis, A. Kokalj, M. Lazzeri, L. Martin-Samos, N. Marzari, F. Mauri, R. Mazzarello, S. Paolini, A. Pasquarello, L. Paulatto, C. Sbraccia, S. Scandolo, G. Sclauzero, A. P. Seitsonen, A. Smogunov, P. Umari and R. M. Wentzcovitch, *J. Phys. Condens. Matter*, 2009, **21**, 395502.
55 S. Maintz, V. L. Deringer, A. L. Tchougreeff and R. Dronskowski, *J. Comput. Chem.*, 2016, **37**, 1030–1035.
56 H. Suzuki, M. Higashi, O. Tomita, Y. Ishii, T. Yamamoto, D. Kato, T. Kotani, D. Ozaki, S. Nozawa, K. Nakashima, K. Fujita, A. Saeki, H. Kageyama and R. Abe, *Chem. Mater.*, 2021, **33**, 9580–9587.
57 Y. Yang, G. Z. Wang, Q. Deng, S. H. Kang, D. H. L. Ng and H. J. Zhao, *CrystEngComm*, 2014, **16**, 3091–3096.
58 S. M. Fray, C. J. Milne and P. Lightfoot, *J. Solid State Chem.*, 1997, **128**, 115–120.
59 D. Kato, K. Hongo, R. Maezono, M. Higashi, H. Kunioku, M. Yabuuchi, H. Suzuki, H. Okajima, C. C. Zhong, K. Nakano, R. Abe and H. Kageyama, *J. Am. Chem. Soc.*, 2017, **139**, 18725–18731.
60 Z. K. Tang, W. J. Yin, L. Zhang, B. Wen, D. Y. Zhang, L. M. Liu and W. M. Lau, *Sci. Rep.*, 2016, **6**, 32764.
61 Y. G. Zhou, L. J. Zhou, J. J. He and T. Frauenheim, *J. Phys. Chem. Lett.*, 2020, **11**, 3095–3102.
62 D. Ozaki, H. Suzuki, K. Ogawa, R. Sakamoto, Y. Inaguma, K. Nakashima, O. Tomita, H. Kageyama and R. Abe, *J. Mater. Chem. A*, 2021, **9**, 8332–8340.
63 Y. Miseki, H. Kusama, H. Sugihara and K. Sayama, *Chem. Lett.*, 2010, **39**, 846–847.
64 H. Suzuki, O. Tomita, M. Higashi and R. Abe, *J. Mater. Chem. A*, 2017, **5**, 10280–10288.

65 K. Ogawa, A. Nakada, H. Suzuki, O. Tomita, M. Higashi, A. Saeki, H. Kageyama and R. Abe, *ACS Appl. Mater. Interfaces*, 2019, **11**, 5642–5650.
66 Y. O. Wang, H. Suzuki, J. J. Xie, O. Tomita, D. J. Martin, M. Higashi, D. Kong, R. Abe and J. W. Tang, *Chem. Rev.*, 2018, **118**, 5201–5241.
67 H. Kato, Y. Sasaki, N. Shirakura and A. Kudo, *J. Mater. Chem. A*, 2013, **1**, 12327–12333.